Critical fields and vortex pinning in overdoped $Ba_{0.2}K_{0.8}Fe_2As_2$

B. Shen,[1] M. Leroux,[1] Y. L. Wang,[1] X. Luo,[1] V. K. Vlasko-Vlasov,[1] A. E. Koshelev,[1] Z. L. Xiao,[1] U. Welp,[1] W. K. Kwok,[1]
M. P. Smylie,[1] A. Snezhko,[1] and V. Metlushko[2]

[1]*Materials Science Division, Argonne National Laboratory, Argonne, Illinois 60439, USA*

[2]*Department of Electrical and Computer Engineering, University of Illinois at Chicago, Chicago, Illinois 60607, USA*

We determine the upper and lower critical fields, the penetration depth and the vortex pinning characteristics of single crystals of overdoped $Ba_{0.2}K_{0.8}Fe_2As_2$ with $T_c \sim 10$ K. We find that bulk vortex pinning is weak and vortex dynamics to be dominated by the geometrical surface barrier. The temperature dependence of the lower critical field, H_{c1}, displays a distinctive upturn at low temperatures, which is suggestive of two distinct superconducting gaps. Furthermore, the penetration depth, λ, varies linearly with temperature below 4 K indicative of line nodes in the superconducting gap. These observations can be well described in a model based on a multiband nodal superconducting gap.

I. INTRODUCTION

The unconventional pairing symmetry and superconducting mechanism of the recently discovered Fe-based superconductors have attracted great attention [1]. Among them, hole-doped $Ba_{1-x}K_xFe_2As_2$ is particularly interesting as it is the first member of the so-called 122 family [2] with the highest transition temperature among all 122 materials at $T_c \sim 38$ K near optimum doping ($x \sim 0.4$). This high T_c, in conjunction with generally high values of the critical current density [3], low superconducting anisotropy [4], and extraordinarily high upper critical fields [5] makes this material promising for applications [6]. However, the nature of the superconducting pairing and the symmetry of the order parameter in these remarkable materials remain rather uncertain. In optimally doped $Ba_{1-x}K_xFe_2As_2$ most experiments suggest an almost isotropic superconducting gap [7–10]. Pairing is reported to be mediated by spin fluctuations [11], which yields a full superconducting gap of $s_{\pm}$ symmetry with opposite signs of the order parameter on the hole Fermi surface sheets centered on the Γ point of the Brillouin zone, and on the electron Fermi surface sheets centered on the X point. In contrast to the doping phase diagram seen in many other iron-based superconductors where the fully doped state is nonsuperconducting, the fully doped material ($x = 1$), KFe_2As_2, is a superconductor with $T_c \sim 3$ K [12]. Furthermore, quantum oscillation measurements [13] show that in KFe_2As_2 the electron Fermi surface sheets have been replaced by narrow cylindrical hole sheets that are slightly displaced from the X point. Thus, with increasing hole doping the Fermi surface of $Ba_{1-x}K_xFe_2As_2$ undergoes significant reconstruction in a Lifshitz transition that occurs in the neighborhood of $x \sim 0.8$ [14–19]. Magnetic penetration depth [20,21], thermal transport [22–25], heat capacity [26–29], and ARPES measurements [16,17] on heavily doped $Ba_{1-x}K_xFe_2As_2$ indicate the presence of line nodes in the superconducting gap. However, the detailed structure and symmetry of the gap are still under debate.

Here we present a comprehensive study of the upper and lower critical fields, and of vortex pinning in single-crystal $Ba_{0.2}K_{0.8}Fe_2As_2$ with $T_c \simeq 10$ K and a doping level slightly above the Lifshitz point. We observe a linear temperature dependence of the penetration depth at low temperatures,

which indicates line nodes in the gap. Micro-Hall probe magnetometry and magneto-optical imaging show that vortex behavior is almost entirely determined by surface barriers with very weak pinning in the bulk. Consequently, the magnetization curves are characterized by a sharp break at an applied magnetic field of H_p when vortices penetrate into the sample. We deduce the c-axis lower critical field, H_{c1}, from H_p using the formalism developed by Brandt [30] and estimate a value of $H_{c1}(0) \sim 360$ Oe. The temperature dependence of H_{c1} is characterized by a distinctive upturn at temperatures below ~ 2 K. Although extrinsic effects related to the mechanism of vortex penetration could produce this feature in $H_{c1}(T)$, in our case the intrinsic nature of this upturn is supported by the consistency with the independently measured temperature dependence of the penetration depth. The upturn in H_{c1} can be very accurately reproduced by an appropriate choice of the zero-temperature penetration depth. In addition, the penetration depth has a linear temperature dependence at low temperatures. These observations can be well described in a model based on a multiband nodal superconducting gap. The upper critical field, H_{c2}, is determined from magnetoresistance measurements yielding slopes of $\mu_0 dH_{c2}{}^c/dT = -1.67$ T/K and $\mu_0 dH_{c2}{}^{ab}/dT = -6$ T/K near T_c implying a rather low anisotropy of the coherence length of $\Gamma \sim 3.6$.

II. EXPERIMENT

Single crystals of heavily overdoped $Ba_{0.2}K_{0.8}Fe_2As_2$ were grown using a self-flux method [31,32]. Selected crystals were characterized by single-crystal x-ray diffraction and a commercial SQUID magnetometer. X-ray diffraction measurements show good crystalline order and SQUID magnetization measurements display sharp superconducting transitions of our samples. The ratio of Ba:K is 0.8:0.2, as determined by energy-dispersive x-ray spectroscopy. The crystals for magneto-optical imaging (MO) and Hall probe magnetometry have dimensions of $400 \times 329 \times 16$ μm^3 and $270 \times 102 \times 20$ μm^3, respectively. The sample used for tunnel diode oscillator (TDO) measurements has an irregular shape. Magneto-optical (MO) imaging experiments of the vortex distribution in the sample were performed in a ⁴He
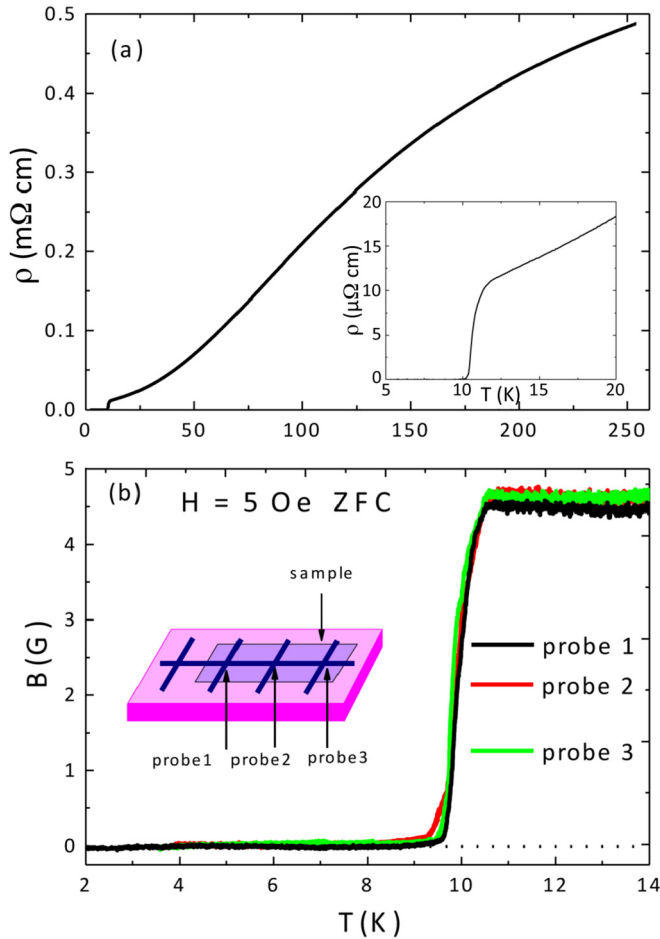
FIG. 1. (Color online) (a) Temperature dependence of resistivity of overdoped $Ba_{0.2}K_{0.8}Fe_2As_2$. The enlarged view of resistivity near superconducting transition is shown in inset of (a). (b) Temperature dependence of magnetic induction at three different positions on the sample. Inset: A schematic of the sample placed on the micro-Hall probe array.
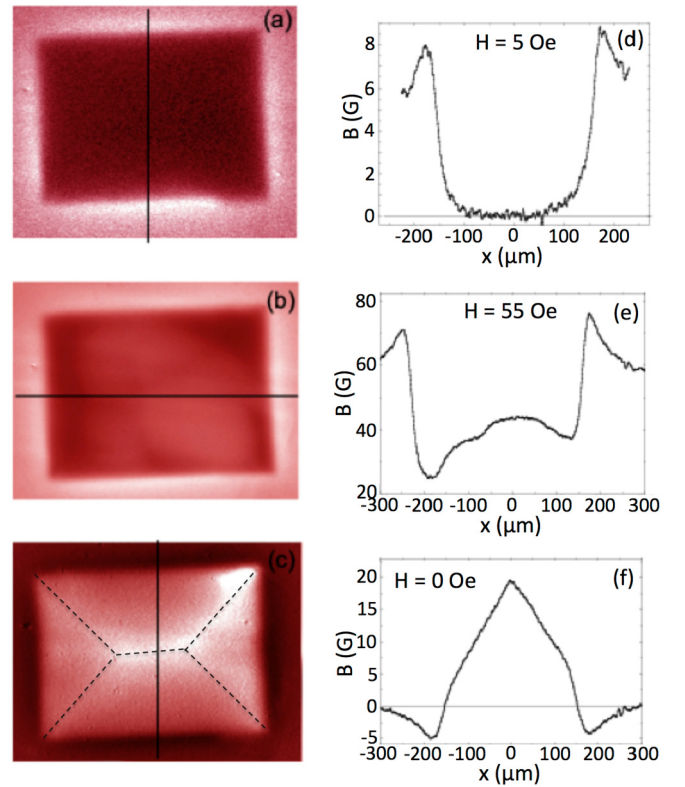

FIG. 2. (Color online) MO image of Meissner shielding (a) and the corresponding magnetic induction (d) at 5 Oe. MO image of flux penetration (b) and the corresponding magnetic induction (e) at 55 Oe at 4.2 K. (c) MO map of the remnant (trapped) flux (c) the corresponding magnetic induction (f) at 0 Oe flux at 4.2 K. The solid lines in the MO images indicate the location of the field profiles. The dotted lines in (c) mark the pillow shape of the flux pattern.

flow-type optical cryostat utilizing the Faraday rotation of linear polarized light in a doped iron-garnet ferrimagnetic indicator film with in plane magnetization placed on top of the crystal [33]. Before performing the experiments, the crystal was cleaved to acquire a fresh surface and immediately loaded into the cryostat to avoid surface degradation due to air. Local magnetization measurements were performed using a two-dimensional (2D) electron gas-based micro-Hall sensor array with four inline sensors of $8 \times 8 \mu m^2$ active areas spaced at 40 μm. The sample was placed onto the array with a thin grease layer [see inset of Fig. 1(b)] such that the edge of the crystal was less than 15 μm away from the nearest Hall sensor. Measurements of the temperature dependence of the penetration depth were conducted using the tunnel diode oscillator (TDO) technique employing a 14-MHz resonator operating in a He-3 cryostat.

III. RESULTS AND DISCUSSION

The temperature-dependent resistivity of $Ba_{0.2}K_{0.8}Fe_2As_2$ is shown in Fig. 1(a): The superconducting transition

temperature is 10.6 K (onset) with a transition width (ΔTc) $\leqslant$ 1 K [inset in Fig. 1(a)]. The high purity of the sample is indicated by the rather large residual resistivity ratio [RRR $\equiv$ $\rho(250 \text{ K})/\rho(10.3 \text{ K})$] of 48. The temperature dependence of the local magnetization at the three locations of the Hall probes is shown in Fig. 1(b). The perfect diamagnetic screening at low temperatures in all three locations indicates homogeneous superconductivity in our sample. The difference in the T_c and the ΔT_c at the three positions is less than 0.01 K (onset of the transition) and 0.2 K, respectively, which demonstrates homogeneous superconductivity in our sample. Figures 2(a)–2(c) show the MO images and the corresponding magnetic induction profiles [Figs. 2(e)–2(f)] obtained in zero-field cooled mode at $T = 4.2$ K. The perfect Meissner shielding, which occurs prior to vortex penetration, is shown in Figs. 2(a) and 2(e) for an applied field of 5 Oe. The high intensity at the edges of the crystal is caused by the strong self-fields generated by the shielding currents. Upon penetration, vortices rapidly move to the center of the sample [shown in Fig. 2(b)]. The maximum magnetic induction of $B_z(x) = 42$ G is observed at the center of the sample and the field profile is dome shaped [see Fig. 2(e)]. For strong bulk pinning a minimum should be observed at the center of the sample since vortices remain pinned near the edge on increasing field. In contrast, vortex accumulation at the

center is a manifestation of weak bulk pinning and the platelike geometry of our sample [34]. Figures 2(c) and 2(f) show the MO image and the magnetic induction profile of trapped flux after the application and withdrawal of 1000 Oe. Except for the bright contrast in the top right corner, which is due to a slight bend of the crystal, the trapped flux distribution is reminiscent of a faint Bean critical state. In particular, the characteristic pillow shape of the field map can be seen. This pattern arises in a platelike sample due to turns in the supercurrent flow that are imposed by the sample shape [33,35]. In Fig. 2(c) the lines on which the current turns bisect the corners indicating that the critical currents are isotropic in the *ab* plane. The critical current density, J_c, associated with this critical state can be estimated from the field profile [Fig. 2(f)] showing the normal component, B_z, of the magnetic induction near the sample surface measured along the line indicated in Fig. 2(c). This profile displays the characteristic features of the critical state in a platelike sample, namely a sharp positive maximum at the center and negative minima of B_z at the sample edges. In general, B_z can be obtained from integrating Biot-Savart's law for the supercurrent pattern in the sample. For a sample in the shape of a long strip (length l, width w and thickness t, $l\, w \gg t$) in a field perpendicular to the surface, B_z is given in closed form. In particular, one finds [36] for the difference ΔB_z of the fields at the edges and in the center $\Delta B_z \approx 3\mu_0 J_c t/2\pi \ln(w/2^{4/3}z_0)$. Here, z_0 is the distance between the magneto-optical indicator film and the sample surface, which typically originates from an uneven sample surface. Using the ratio, r, of the field at the center and at the edges of the sample, $r \approx -2\ln(w/2z_0)/\ln(w/4z_0)$, we can estimate z_0 from the data in Fig. 2(f) as $z_0 \sim 30\,\mu$m. This value is consistent with the rounding seen on the peaks of B_z at the sample edges. In this analysis, we approximated the sample as a sheet current $J_c t$ located at a distance z_0, an approximation that is justified since $z_0 > t$. We then obtain a critical current density of $J_c \sim 18$ kA/cm^2 at 4 K. This value of J_c is more than two orders of magnitude lower than typically seen for optimally doped Ba$_{1-x}$K$_x$Fe$_2$As$_2$ [3] indicating that pristine Ba$_{0.2}$K$_{0.8}$Fe$_2$As$_2$ has very low bulk pinning. The evolution of pinning with doping mirrors the behavior previously reported in BaFe$_2$(As$_{1-x}$P$_x$)$_2$ [37]. For both families of superconductors the parent compounds, KFe$_2$As$_2$ and BaFe$_2$P$_2$, form crystals of very high purity displaying residual resistivity ratios of 600 [38] to 1280 [21], and $\sim$85 [39], respectively. Thus, by increasing the doping level the purity increases and, at the time, bulk pinning rapidly decreases.

IV. SURFACE BARRIER EFFECTS AND LOWER CRITICAL FIELD

The low bulk pinning is evident in the magnetization hysteresis loops obtained with Hall probe magnetometry as shown in Fig. 3. On initially increasing field, the linear *M-H* variation corresponding to the Meissner state is observed. At an applied field H_p a sharp cusp in $M(H)$ occurs signaling the penetration of vortices into the sample. On reducing the applied field from a maximum field of 1000 Oe the magnetization stays close to zero until a small remnant field of $\sim$60 Oe is reached. This remnance corresponds to the trapped field shown in Fig. 2(c) and a critical current density of ~ 18 kA/cm^2. In
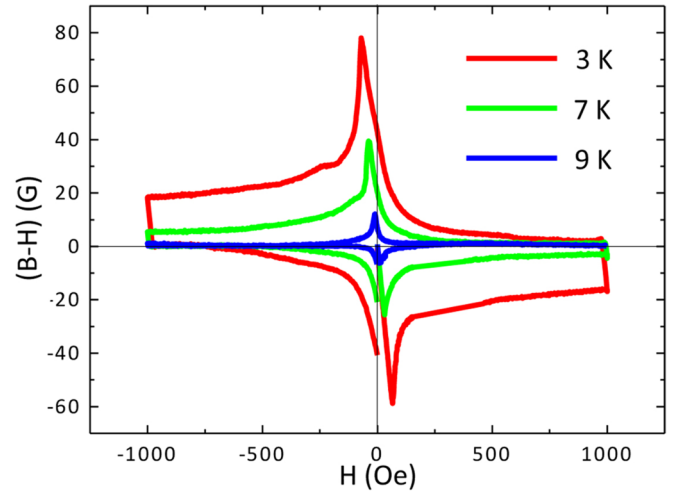

FIG. 3. (Color online) Magnetization hysteresis loops measured with Hall sensor 1 at various temperatures.

contrast to strong-pinning superconductors the magnetization hysteresis loops shown in Fig. 3 display a characteristic anisotropy about the field axis, which is the signature of vortex dynamics dominated by surface barriers [30,40,41].

In general, the penetration of vortices into the sample is a nonequilibrium process, and the apparent penetration field is related to the thermodynamic lower critical field in a nontrivial way. At least two effects inhibit vortex entry, the microscopic Bean-Livingston surface barrier [42] and the so-called geometrical or edge barrier that arises in platelike samples [34,40], each being characterized by a vortex penetration field H_p^{BL} and H_p^{GB}, respectively. A recent theoretical study [43] showed that the interplay between these barriers leads to two regimes of vortex penetration. For a strong surface barrier, $H_p^{BL} > H_p^{GB}$, vortices nucleate at the corners at H_p^{BL} and then immediately move to the sample center. For an ideal corner and negligible creep $H_p^{BL} \approx H_c(144t\lambda^2/\pi w^3)^{1/6}$, where H_c is the thermodynamic critical field. In the case of a weak surface barrier, $H_p^{BL} < H_p^{GB}$, vortex penetration occurs in two stages: after nucleation at $H = H_p^{BL}$ vortices first reside in the corners and jump to the center only at higher field, $H_p^{GB} > H_p^{BL}$. Thus, in this two-stage process there appears a vortex-filled rim along the sample edges with a width that is of the order of the sample thickness [43]. The contrast seen in Figs. 2(a) and 2(d) along the inside edge of the sample could be a manifestation of this effect convoluted with the optical resolution. A detailed numerical analysis of the geometrical barrier regime by Brandt for an isotropic superconducting slab yields $H_p^{GB} = H_{c1} \tanh(\sqrt{\alpha t/w})$ with $\alpha = 0.36$ for long strips and $\alpha = 0.67$ for discs, w and t are the width and thickness of the sample, respectively [30]. This result can be generalized [47] to anisotropic superconductors using an expansion of the formalism given in Ref. [43]: $H_p^{GB} \approx \sqrt{(4t/\pi w)/[1 + (2\Gamma/\pi)^{2/3}]}\, H_{c1}^c$, where H_{c1}^c is the *c*-axis lower critical field and $\Gamma \gg 1$ is the anisotropy factor, and $t \ll w$. A numerical solution shows that for $\Gamma \sim 3$ this expansion overestimates the reduction of the penetration field by $\sim$4%. A quantitative analysis of experimental data according to this relation is complicated by the fact that in real samples irregularities and defects at the

edges have a strong effect on vortex penetration. For instance, estimated materials parameters of $Ba_{0.2}K_{0.8}Fe_2As_2$ would formally place this material in the regime of predominant Bean-Livingston surface barrier, $H_p^{BL} > H_p^{GB}$. Following [43], the relation between H_p^{BL} and H_{c1} is given as $H_P^{BL} \approx 1.53 H_{c1} \sqrt{m} / \ln(\kappa) \lambda / \xi (\lambda/t)^{1/3}$, where $m = 4t/\pi w$ describes the aspect ratio of the sample. Expressing this relation in terms of H_{c1} only and attributing the observed penetration field to the ideal H_p^{BL} yields an unreasonably small value of $H_{c1} \sim 11$ Oe. Here we used for the coherence length $\xi = 4$ nm (see below) and assumed $k \sim 40$ (since κ enters only under the logarithm an error in κ would not affect above estimate in any significant way). The Bean-Livingston barrier is very sensitive to surface conditions [44], and as our samples are cut from a layered, micaceous material the sides of the samples are rough on the scale of λ such that numerous gates [45] arise allowing vortices to pass through the Bean-Livingston barrier. Here, we assume that H_p^{BL} is suppressed below H_p^{GB} by surface roughness and deduce the lower critical field H_{c1} from the penetration field H_p^{GB} using the procedure outlined in Refs. [30,43,46], including the correction due to anisotropy.

We determine the penetration field using two methods: (i) from the sharp cusps in the zero-field cooled magnetization $M(H)$ [Fig. 4(a)], (ii) from measurements of the remnant local
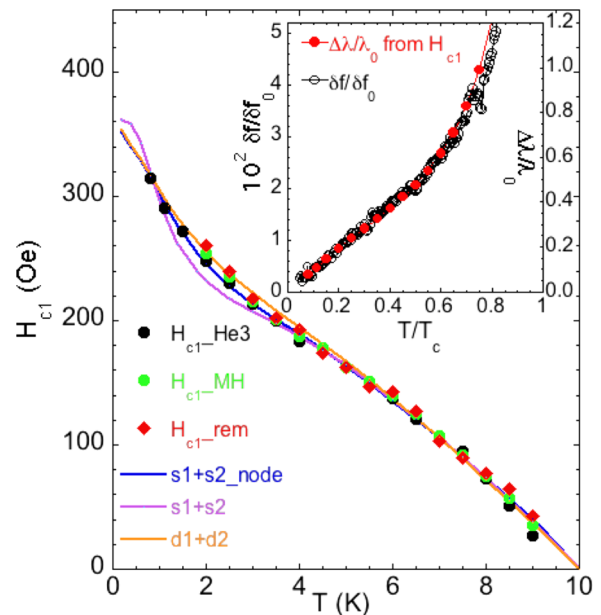
FIG. 5. (Color online) The temperature-dependent H_{c1} determined from magnetization curves (black and green circles) and from the remnant field (red diamonds). Fitting: (purple line) two s-wave gaps, (blue line) s-wave and nodal s-wave gaps, (orange line) two d-wave gaps. Inset: Temperature dependence of the normalized resonance frequency of the tunnel diode oscillator plotted together with the change in penetration depth calculated using a fourth-order polynomial fit of the H_{c1} data in the main panel.

field $B_{\rm rem}$ in the sample after applying a magnetic field H and then sweeping the field back to zero [46]. $B_{\rm rem}$ will remain equal to zero in the Meissner state and start increasing sharply when the first vortices enter at H_p [Fig. 4(b)]. Figure 5 shows the temperature dependence of the resulting values for H_{c1}. For $T \gtrsim 4$ K, $H_{c1}(T)$ follows a conventional temperature dependence extrapolating to $H_{c1} = 0$ at $T \sim 10$ K, whereas, below ~ 2 K, $H_{c1}(T)$ displays a distinctive upturn with a zero-temperature value of $H_{c1}(0) \sim 360$ Oe. Such behavior has been observed previously, e.g., for cuprate high-temperature superconductors, and has been attributed to thermal creep in the presence of bulk pinning and surface barrier effects [45,48]. These effects cannot be ruled out completely in our study, and pinning on rough side faces of the sample could lead to an enhanced geometrical barrier and enhanced apparent H_{c1}. In addition, reported Hall probe magnetometry measurements of the penetration field of $PrFeAsO_{1-y}$ [49] revealed that the results depend on the location of the Hall sensor with respect to the sample edge. Readings from the sample center yielded significantly higher values of the apparent penetration field and an upturn at low temperatures, which was not seen in readings taken close to the sample edge. Such behavior may be expected since the $PrFeAsO_{1-y}$ crystal displayed sizable bulk pinning. In contrast, our $Ba_{0.2}K_{0.8}Fe_2As_2$ crystal has very low bulk pinning mitigating such behavior. Furthermore, a comparison with measurements of the temperature dependence of the penetration depth (see below) suggests that in the case of $Ba_{0.2}K_{0.8}Fe_2As_2$ the temperature variation of H_{c1} shown in Fig. 5 is a reflection of the intrinsic superconducting gap structure. We also note that μSR experiments, which are
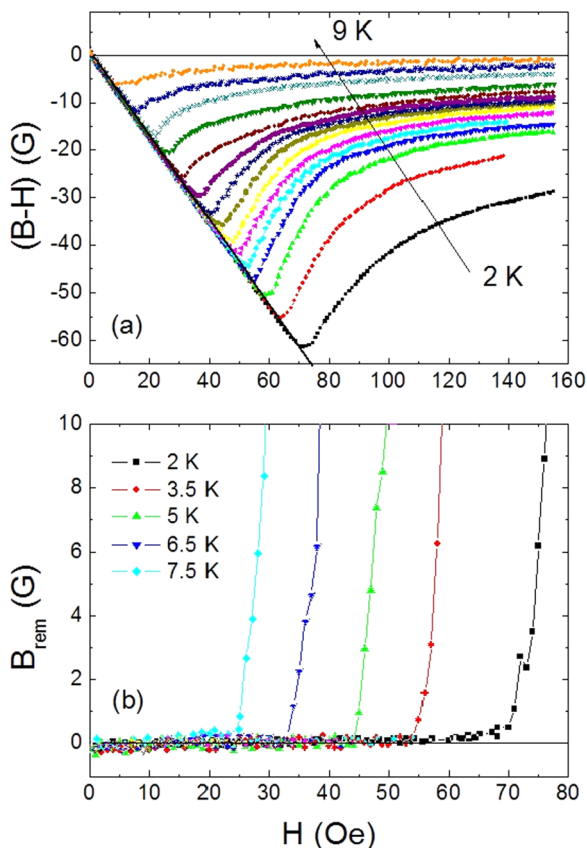

FIG. 4. (Color online) (a) The field dependence of local magnetization (at probe 1) in ZFC measurements measured at various temperatures between 2 K and 9 K at 0.5 K temperature increments. (b) The remnant induction at various temperatures measured with Hall sensor 1 as a function of applied peak field.

insensitive to vortex penetration and vortex pinning phenomena, revealed a low-temperature upturn in the superfluid density of near-optimum doped $Ba_{1-x}K_xFe_2As_2$, which was interpreted as signature of two-gap superconductivity [50]. The change of the penetration depth of the sample is proportional to the frequency shift seen in TDO [51]: $\Delta\lambda/\lambda_0 = G\delta f/\delta f_0$. Here $\Delta\lambda = \lambda(T) - \lambda_0$ and λ_0 is the zero-temperature penetration length; δf_0 is the total frequency shift between T_c and the lowest temperature; G is a geometrical factor that depends upon the sample shape and volume as well as the coil geometry of the TDO system [51]. The inset of Fig. 5 displays the temperature dependence of the normalized resonance frequency shift $\delta f/\delta f_0$. At low temperatures the data show clear linear behavior, which corresponds to a linear temperature dependence of $\Delta\lambda/\lambda_0$ and is indicative of nodes in the superconducting gap [52]. In fact, $\Delta\lambda/\lambda_0$ can be obtained independently from the measured $H_{c1}(T)$ data using the Ginzburg-Landau relation $H_{c1} = \Phi/4\pi\lambda^2[\ln\kappa_3 + 0.5]$. κ_3 is the weakly temperature-dependent third Ginzburg-Landau parameter, which in the Ginzburg-Landau regime near T_c becomes equal to $\kappa = \lambda/\xi$ [53]. Here, we neglect the weak temperature dependence under the logarithm. Then both data sets, $\Delta\lambda(T)/\lambda_0$ as determined from H_{c1} and $\delta f/\delta f_0$, can be mapped exactly onto each other over a wide temperature range as shown in the inset of Fig. 5 indicating that both measurements yield a consistent determination of the temperature dependence of H_{c1}. From the y scales in the inset one can estimate a geometrical factor of $G \sim 25$ [54]. The linear temperature variation of $\Delta\lambda/\lambda_0$ is consistent with the high purity of the sample, as strong impurity scattering would induce a T^2 dependence in λ [52]. Similar results have been reported recently for a series of overdoped $Ba_{1-x}K_xFe_2As_2$ crystals [20]. The superfluid density is given as $\rho_s = \lambda_0^2/\lambda(T)^2 \approx H_{c1}(T)/H_{c1}(0)$. We use various models for the superconducting gap structure to fit the temperature dependence of ρ_S, that is, of H_{c1}. The superfluid density of a two-dimensional (2D) cylindrical Fermi surface is given as [55]:

$$\rho = 1 - \frac{1}{2\pi T}\int_0^{2\pi}\cos^2\phi\int_0^\infty \cos h^{-2}\frac{\sqrt{\epsilon^2 + \Delta(T)^2}}{2T}d\epsilon d\phi$$

with the gap function $\Delta(T) = \Delta_0\tanh\left(\frac{\pi T_c}{\Delta_0}\sqrt{\alpha(\frac{T_c}{T} - 1)}\right)g(\phi)$. Here, Δ_0 is the gap magnitude at zero temperature and α is a parameter dependent on the particular pairing state. For example, for clean d-wave symmetry, $g(\phi) = \cos(2\phi), \alpha = 4/3$, and for nodal s-wave $g = |\cos(4\phi v)|$ and $\alpha = 1$ [17]. Single-band models do not account for the observed upturn of H_{c1} at low temperatures. Therefore, we fit the H_{c1} data by using various two-band models. For a superconductor with two gaps, the normalized superfluid density may be written approximately as $\rho_s = \gamma_1\rho_1 + \gamma_1\rho_2$ where $\gamma_1 + \gamma_2 = 1$ are the fractions of superfluid density and $\rho_i(i = 1,2)$ is the superfluid

TABLE I. Fit parameters.

Model	$\Delta_1(0)$ (meV)	γ_1	$\Delta_2(0)$ (meV)	γ_2
$s_1 + s_2$	1.5	0.57	0.2	0.43
$s_1 + s_{2,nodal}$	1.5	0.5	0.4	0.5
$d_1 + d_2$	2	0.65	0.3	0.35

density on different Fermi surface sheets. Although this procedure neglects possible modifications of the temperature dependence of the gaps due to multiband effects and is therefore not self-consistent [56], it has proven useful to describe experimental data of the specific heat or superfluid density of multiband superconductors [57]. The fitting results and parameters are shown in Fig. 5 and Table I.

The results obtained here are in overall agreement with recent ARPES measurements [16,17] on heavily overdoped $Ba_{1-x}K_xFe_2As_2$. Those measurements indicate the
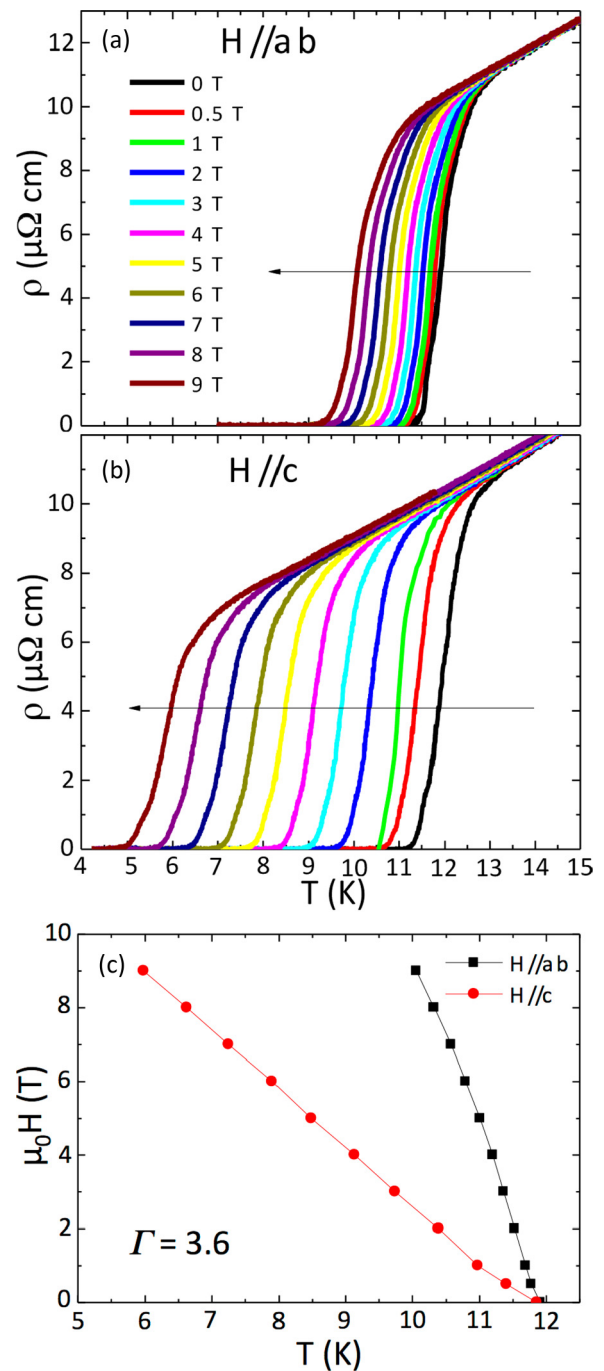

FIG. 6. (Color online) (a), (b) Resistive transitions in various magnetic fields applied along the ab planes and along the c axis, respectively. (c) The H_{c2} phase diagram of $Ba_{0.2}K_{0.8}Fe_2As_2$.

simultaneous appearance of Fermi surface sheets with nodal gaps and with complete gaps. Although there are discrepancies regarding the exact gap structure [16,17], they bear out the general feature of large complete gaps coexisting with small nodal (or highly anisotropic) gaps and are consistent with the results of the fits of our H_{c1} data. Furthermore, from the H_{c1} measurements and its fits we can directly deduce the corresponding temperature variation of the penetration depth, which is also included in the inset of Fig. 5. At temperatures below 7 K, the deduced $\Delta\lambda/\lambda_0$ dependence agrees very well with the measured $\delta f/\delta f_0$ data indicating that both measurement techniques yield consistent results and that the upturn in H_{c1} is an intrinsic property caused by the structure of the superconducting gap. As can be seen from Fig. 5, fits according to the $s_1 + s_{2,\text{nodal}}$ and the $d_1 + d_2$ models describe the data equally well; with our current resolution we cannot distinguish these two gap symmetries.

V. UPPER CRITICAL FIELD

Figures 6(a) and 6(b) show the resistive transitions measured in magnetic fields applied along the *ab* plane and along the *c* axis, respectively, for a crystal with a slightly higher value of T_c. The superconducting transitions are sharp and shift uniformly with field to lower temperature without any significant field-induced broadening. Similar results were recently reported in a study on a series of overdoped $Ba_{1-x}K_xFe_2As_2$ samples [32]. Weak broadening is indicative for high sample homogeneity and weak effects due to superconducting fluctuations. The small contribution of superconducting fluctuations can be inferred from the small value of the Ginzburg number [58] $G_i = (k_B\mu_0\Gamma T_c/4\pi\xi^3 B_c^2)^2/2 \approx 323.3(\Gamma\kappa\lambda T_c)^2$, where we have employed the Ginzburg-Landau relations for an effective single-band superconductor, and λ is measured in meters. k_B is the Boltzmann constant, μ_0 the permeability of vacuum, Γ the anisotropy of the coherence length, B_c the thermodynamic critical field, and ξ is the in-plane coherence length. With $\Gamma \sim 3.6$ and $k \sim 40$ as determined below, we find $G_i \sim 10^{-4}$. This value is significantly smaller than that of optimally doped $Ba_{1-x}K_xFe_2As_2$ and $BaFe_2(As_{1-x}P_x)_2$ for which $G_i \sim 10^{-3}$ [4,59] and of the more anisotropic $SmFeAsO_{0.85}F_{0.15}$ and $NdFeAsO_{0.82}F_{0.18}$ compounds with $G_i \sim 10^{-2}$ [60,61].

Using the resistive midpoints as criterion we obtain the H_{c2} phase diagram as shown in Fig. 6(c). Near T_c, $H_{c2}(T)$ is linear with slopes of $\mu_0 dH_{c2}{}^c/dT = -1.67$ T/K

and $\mu_0 dH_{c2}{}^{ab}/dT = -6$ T/K yielding an anisotropy of the coherence length of $\Gamma \sim 3.6$. This rather low value of the anisotropy is most likely due to a sizable *c*-axis dispersion of the middle hole sheet around the Γ point [13]. Using the Ginzburg-Landau relation for a single-band superconductor we estimate an effective in-plane coherence length of $\xi \sim 4$ nm and a Ginzburg-Landau parameter of $k \sim 40$. For the in-plane orientation, $H_{c2}(T)$ shows clear downwards deviation from the linear temperature dependence resulting in an anisotropy Γ that decreases with decreasing temperature. Such behavior has been reported for several Fe-based superconductors [5,62] and is probably a signature of paramagnetic limiting. On the other hand, a weak upward curvature of $H_{c2}{}^c$ near T_c may be a signature of multiple-band effects [63].

VI. CONCLUSIONS

In summary, we determine the vortex pinning characteristics, the upper and lower critical fields, and the penetration depth of single crystals of overdoped $Ba_{0.2}K_{0.8}Fe_2As_2$ with $T_c \sim 10$ K and a doping level slightly above the Lifshitz point. Bulk vortex pinning was found to be exceedingly weak, such that vortex dynamics is entirely dominated by the geometrical surface barrier. Under such conditions, H_{c1} can be determined from the field of first vortex penetration. We deduce the *c*-axis value of $H_{c1}(0) \sim 360$ Oe, corresponding to an in-plane penetration depth of $\lambda_{ab}(0) \sim 140$ nm. The temperature dependence of the H_{c1} displays a distinctive upturn below ~ 2 K, which is consistent with the observed linear temperature dependence of the penetration depth and which can be well described in a model of a multiband nodal superconducting gap.

[1] Y. Kamihara, T. Watanabe, M. Hirano, and H. Hosono, J. Am. Chem. Soc. **130**, 3296 (2008); H. Takahashi, K. Igawa, K. Arii, Y. Kamihara, M. Hirano, and H. Hosono, Nature (London) **453**, 376 (2008); J. Paglione and R. L. Greene, Nature Phys. **6**, 645 (2010); H . H. Wen and S. Li, Annu. Rev. Condens. Matter Phys. **2**, 121 (2011); P. C. Canfield and S. L. Bud'ko, *ibid.* **1**, 27 (2011); D. C. Johnston, Adv. Phys. **59**, 803 (2010).

[2] M. Rotter, M. Tegel, and D. Johrendt, Phys. Rev. Lett. **101**, 107006 (2008).

[3] B. Shen, P. Cheng, Z. S. Wang, L. Fang, C. Ren, L. Shan, and H.-H. Wen, Phys. Rev. B **81**, 014503 (2010); R. Prozorov, M. A. Tanatar, B. Roy, N. Ni, S. L. Bud'ko, P. C. Canfield, J. Hua, U. Welp, and W. K. Kwok, *ibid.* **81**, 094509 (2010); L. Fang, Y. Jia, C. Chaparro, G. Sheet, H. Claus, M. A. Kirk, A. E. Koshelev, U. Welp, G. W. Crabtree, W. K. Kwok, S. Zhu, H. F. Hu, J. M. Zuo, H.-H. Wen, and B. Shen, Appl. Phys. Lett. **101**, 012601 (2012); K. J. Kihlstrom, L. Fang, Y. Jia, B. Shen, A. E. Koshelev, U. Welp, G. W. Crabtree, W.-K. Kwok, A. Kayani, S. F. Zhu, and H.-H. Wen, *ibid.* **103**, 202601 (2013).

[4] Z.-S. Wang, H.-Q. Luo, C. Ren, and H.-H. Wen, Phys. Rev. B **78**, 140501 (2008); G. F. Chen, Z. Li, J. Dong, G. Li, W. Z. Hu, X. D. Zhang, X. H. Song, P. Zheng, N. L. Wang, and J. L. Luo, *ibid.* **78**, 224512 (2008); U. Welp, R. Xie, A. E. Koshelev, W. K. Kwok, H. Q. Luo, Z. S. Wang, G. Mu, and H. H. Wen, *ibid.* **79**, 094505 (2009).

[5] M. M. Altarawneh, K. Collar, C. H. Mielke, N. Ni, S. L. Bud'ko, and P. C. Canfield, Phys. Rev. B **78**, 220505 (2008); H. Q. Yuan, J. Singleton, F. F. Balakirev, S. A. Baily, G. F. Chen, J. L. Luo, and N. L. Wang, Nature (London) **457**, 565 (2009).

[6] J. D. Weiss, C. Tarantini, J. Jiang, F. Kametani, A. A. Polyanskii, D. C. Larbalestier, and E. E. E. Hellstrom, Nature Mater. **11**, 682 (2012); Z. S Gao, K. Togano, A. Matsumoto, and H. Kumakura, Sci. Rep. **4**, 4065 (2014); A. Gurevich, Nature Mater. **10**, 255 (2011).

[7] H. Ding *et al.*, Europhys. Lett. **83**, 47001 (2008); Y-M. Xu, Y-B. Huang, X-Y. Cui, E. Razzoli, M. Radovic, M. Shi, G-F. Chen, P. Zheng, N-L. Wang, C-L. Zhang, P-C. Dai, J-P. Hu, Z. Wang, and H. Ding, Nature Phys. **7**, 198 (2011).

[8] L. Shan, Y. L. Wang, J. Gong, B. Shen, Y. Huang, H. Yang, C. Ren, and H. H. Wen, Phys. Rev. B **83**, 060510 (2011).

[9] X. G. Luo, M. A. Tanatar, J.-Ph. Reid, H. Shakeripour, N. Doiron-Leyraud, N. Ni, S. L. Bud'ko, P. C. Canfield, H. Q. Luo, Z. S. Wang, H.-H. Wen, R. Prozorov, and L. Taillefer, Phys. Rev. B **80**, 140503 (2009); Y. M. Dai, B. Xu, B. Shen, H. H. Wen, X. G. Qiu, and R. P. S. M. Lobo, Europhys. Lett. **104**, 47006 (2013).

[10] C. Martin, R. T. Gordon, M. A. Tanatar, H. Kim, N. Ni, S. L. Bud'ko, P. C. Canfield, H. Luo, H. H. Wen, Z. Wang, A. B. Vorontsov, V. G. Kogan, and R. Prozorov, Phys. Rev. B **80**, 020501 (2009); C. Ren, Z.-S. Wang, H.-Q. Luo, H. Yang, L. Shan, and H.-H. Wen, Phys. Rev. Lett. **101**, 257006 (2008); G. Mu, H.-Q. Luo, Z.-S. Wang, L. Shan, C. Ren, and H.-H. Wen, Phys. Rev. B **79**, 174501 (2009).

[11] I. I. Mazin, D. J. Singh, M. D. Johannes, and M. H. Du, Phys. Rev. Lett. **101**, 057003 (2008); P. J. Hirschfeld, M. M. Korshunov, and I. I. Mazin, Rep. Prog. Phys. **74**, 124508 (2011).

[12] M. Rotter, M. Pangerl, M. Tegel, and D. Johrendt, Angew. Chem., Int. Ed. **47**, 7949 (2008).

[13] T. Terashima, M. Kimata, N. Kurita, H. Satsukawa, A. Harada, K. Hazama, M. Imai, A. Sato, K. Kihou, C.-H. Lee, H. Kito, H. Eisaki, A. Iyo, T. Saito, H. Fukazawa, Y. Kohori, H. Harima, and S. Uji, J. Phys. Soc. Jpn. **79**, 053702 (2010); T. Terashima, N. Kurita, M. Kimata, M. Tomita, S. Tsuchiya, M. Imai, A. Sato, K. Kihou, C.-H. Lee, H. Kito, H. Eisaki, A. Iyo, T. Saito, H. Fukazawa, Y. Kohori, H. Harima, and S. Uji, Phys. Rev. B **87**, 224512 (2013).

[14] W. Malaeb, T. Shimojima, Y. Ishida, K. Okazaki, Y. Ota, K. Ohgushi, K. Kihou, T. Saito, C. H. Lee, S. Ishida, M. Nakajima, S. Uchida, H. Fukazawa, Y. Kohori, A. Iyo, H. Eisaki, C.-T. Chen, S. Watanabe, H. Ikeda, and S. Shin, Phys. Rev. B **86**, 165117 (2012).

[15] S. N. Khan and D. D. Johnson, Phys. Rev. Lett. **112**, 156401 (2014).

[16] N. Xu, P. Richard, X. Shi, A. van Roekeghem, T. Qian, E. Razzoli, E. Rienks, G.-F. Chen, E. Ieki, K. Nakayama, T. Sato, T. Takahashi, M. Shi, and H. Ding, Phys. Rev. B **88**, 220508 (2013).

[17] Y. Ota, K. Okazaki, Y. Kotani, T. Shimojima, W. Malaeb, S. Watanabe, C.-T. Chen, K. Kihou, C. H. Lee, A. Iyo, H. Eisaki,

T. Saito, H. Fukazawa, Y. Kohori, and S. Shin, Phys. Rev. B **89**, 081103 (2014); K. Okazaki, Y. Ota, Y. Kotani, W. Malaeb, Y. Ishida, T. Shimojima, T. Kiss, S. Watanabe, C.-T. Chen, K. Kihou, C. H. Lee, A. Iyo, H. Eisaki, T. Saito, H. Fukazawa, Y. Kohori, K. Hashimoto, T. Shibauchi, Y. Matsuda, H. Ikeda, H. Miyahara, R. Arita, A. Chainani, and S. Shin, Science **337**, 1314 (2012).

[18] K. Nakayama, T. Sato, P. Richard, Y.-M. Xu, T. Kawahara, K. Umezawa, T. Qian, M. Neupane, G. F. Chen, H. Ding, and T. Takahashi, Phys. Rev. B **83**, 020501 (2011).

[19] H. Hodovanets, Y. Liu, A. Jesche, S. Ran, E. D. Mun, T. A. Lograsso, S. L. Bud'ko, and P. C. Canfield, Phys. Rev. B **89**, 224517 (2014).

[20] D. Watanabe, T. Yamashita, Y. Kawamoto, S. Kurata, Y. Mizukami, T. Ohta, S. Kasahara, M. Yamashita, T. Saito, H. Fukazawa, Y. Kohori, S. Ishida, K. Kihou, C. H. Lee, A. Iyo, H. Eisaki, A. B. Vorontsov, T. Shibauchi, and Y. Matsuda, Phys. Rev. B **89**, 115112 (2014).

[21] K. Hashimoto, A. Serafin, S. Tonegawa, R. Katsumata, R. Okazaki, T. Saito, H. Fukazawa, Y. Kohori, K. Kihou, C. H. Lee, A. Iyo, H. Eisaki, H. Ikeda, Y. Matsuda, A. Carrington, and T. Shibauchi, Phys. Rev. B **82**, 014526 (2010).

[22] J.-Ph. Reid, M. A. Tanatar, A. Juneau-Fecteau, R. T. Gordon, S. René de Cotret, N. Doiron-Leyraud, T. Saito, H. Fukazawa, Y. Kohori, K. Kihou, C. H. Lee, A. Iyo, H. Eisaki, R. Prozorov, and L. Taillefer, Phys. Rev. Lett. **109**, 087001 (2012).

[23] J.-P. Reid, A. Juneau-Fecteau, R. T. Gordon, S. Rene de Cotret, N. Doiron-Leyraud, X. G. Luo, H. Shakeripour, J. Chang, M. A. Tanatar, H. Kim, R. Prozorov, T. Saito, H. Fukazawa, Y. Kohori, K. Kihou, C. H. Lee, A. Iyo, H. Eisaki, B. Shen, H.-H. Wen, and L. Taillefer, Supercond. Sci. Technol. **25**, 084013 (2012).

[24] A. F. Wang, S. Y. Zhou, X. G. Luo, X. C. Hong, Y. J. Yan, J. J. Ying, P. Cheng, G. J. Ye, Z. J. Xiang, S. Y. Li, and X. H. Chen, Phys. Rev. B **89**, 064510 (2014).

[25] X. C. Hong, A. F. Wang, Z. Zhang, J. Pan, L. P. He, X. G. Luo, X. H. Chen, and S. Y. Li, arXiv:1401.0792.

[26] M. Abdel-Hafiez, V. Grinenko, S. Aswartham, I. Morozov, M. Roslova, O. Vakaliuk, S. Johnston, D. V. Efremov, J. van den Brink, H. Rosner, M. Kumar, C. Hess, S. Wurmehl, A. U. B. Wolter, B. Büchner, E. L. Green, J. Wosnitza, P. Vogt, A. Reifenberger, C. Enss, M. Hempel, R. Klingeler, and S.-L. Drechsler, Phys. Rev. B **87**, 180507(R) (2013).

[27] F. Hardy, R. Eder, M. Jackson, D. Aoki, C. Paulsen, T. Wolf, P. Burger, A. Böhmer, P. Schweiss, P. Adelmann, R. A. Fisher, and C. Meingast, J. Phys. Soc. Jpn. **83**, 014711 (2014).

[28] S. Kittaka, Y. Aoki, N. Kase, T. Sakakibara, T. Saito, H. Fukazawa, Y. Kohori, K. Kihou, C.-H. Lee, A. Iyo, H. Eisaki, K. Deguchi, N. K. Sato, Y. Tsutsumi, and K. Machida, J. Phys. Soc. Jpn. **83**, 013704 (2014).

[29] S. L. Bud'ko, M. Sturza, D. Y. Chung, M. G. Kanatzidis, and P. C. Canfield, Phys. Rev. B **87**, 100509 (2013).

[30] E. H. Brandt, Phys. Rev. B **59**, 3369 (1999); Low Temp. Phys. **27**, 723 (2001).

[31] B. Shen, H. Yang, Z.-S. Wang, F. Han, B. Zeng, L. Shan C. Ren, and H.-H. Wen, Phys. Rev. B **84**, 184512 (2011).

[32] Y. Liu, M. A. Tanatar, W. E. Straszheim, B. Jensen, K. W. Dennis, R. W. McCallum, V. G. Kogan, R. Prozorov, and T. A. Lograsso, Phys. Rev. B **89**, 134504 (2014).

[33] L. Dorosinskii, M. V. Indenbom, V. I. Nikitenko, Yu. A. Ossipyan, A. A. Polyanskii, and V. K. Vlasko-Vlasov, Physica

C **203**, 149 (1992); V. K. Vlasko-Vlasov, G. W. Crabtree, U. Welp, and V. I. Nikitenko, NATO Advanced Science Institutes Series, Series E, Applied Sciences **356**, 205 (1999); U. Welp, V. K. Vlasko-Vlasov, X. Liu, J. K. Furdyna, and T. Wojtowicz, Phys. Rev. Lett. **90**, 167206 (2003).

[34] M. V. Indenbom, H. Kronmüller, T. W. Li, P. H. Kes, and A. A. Menovsky, Physica C **222**, 203 (1994); E. Zeldov, A. I. Larkin, V. B. Geshkenbein, M. Konczykowski, D. Majer, B. Khaykovich, V. M. Vinokur, and H. Shtrikman, Phys. Rev. Lett. **73**, 1428 (1994); Th. Schuster, M. V. Indenbom, H. Kuhn, E. H. Brandt, and M. Konczykowski, *ibid.* **73**, 1424 (1994).

[35] Th. Schuster, H. Kuhn, E. H. Brandt, M. V. Indenbom, M. Kläser, G. Müller-Vogt, H.-U. Habermeier, H. Kronmüller, and A. Forkl, Phys. Rev. B **52**, 10375 (1995); A. A. Polyanskii, A. Gurevich, A. E. Pashitski, N. F. Heinig, R. D. Redwing, J. E. Nordman, and D. C. Larbalestier, *ibid.* **53**, 8687 (1996).

[36] U. Welp, Z. L. Xiao, V. Novosad, and V. K. Vlasko-Vlasov, Phys. Rev. B **71**, 014505 (2005).

[37] L. Fang, Y. Jia, J. A. Schlueter, A. Kayani, Z. L. Xiao, H. Claus, U. Welp, A. E. Koshelev, G. W. Crabtree, and W.-K. Kwok, Phys. Rev. B **84**, 140504 (2011).

[38] H. Fukuzawa, T. Saito, Y. Yamada, K. Kondo, M. Hirano, Y. Kohori, K. Kuga, A. Sakai, Y. Matsumoto, S. Nakatsuji, K. Kihou, A. Iyo, C. H. Lee, and H. Eisaki, J. Phys. Soc. Jpn. **80**, SA118 (2011).

[39] M. Nakajima, S. Uchida, K. Kihou, C.-H. Lee, A. Iyo, and H. Eisaki, J. Phys. Soc. Jpn. **81**, 104710 (2012).

[40] M. Benkraouda and J. R. Clem, Phys. Rev. B **53**, 5716 (1996).

[41] J. R. Clem, in *Proceedings of the 13th Conference on Low Temperature Physics (LT 13)*, edited by K. D. Timmerhaus, W. J. O'Sullivan, and E. F. Hammel (Plenum, New York, 1974), Vol. 3, p. 102; L. Burlachkov, Phys. Rev. B **47**, 8056 (1993).

[42] C. P. Bean and J. D. Livingston, Phys. Rev. Lett. **12**, 14 (1964).

[43] E. H. Brandt, G. P. Mikitik, and E. Zeldov, J. Exper. Theor. Phys. **117**, 439 (2013).

[44] R. W. De Blois and W. De Sorbo, Phys. Rev. Lett. **12**, 499 (1964); M. A. R. LeBlanc, G. Fillion, W. E. Timms, A. Zahradnitsky, and J. R. Cave, Cryogenics **21**, 491 (1981); J. F. Bussiere and M. Suenaga, J. Appl. Phys. **47**, 707 (1976).

[45] L. Burlachkov, Y. Yeshurun, M. Konczykowski, and F. Holtzberg, Phys. Rev. B **45**, 8193 (1992).

[46] M. Leroux, P. Rodiere, L. Cario, and T. Klein, Physica B **407**, 1813 (2012).

[47] A. E. Koshelev (unpublished).

[48] V. N. Kopylov, A. E. Koshelev, I. F. Schegolev, and T. G. Togonidze, Physica C **170**, 291 (1990); L. Burlachkov, V. B. Geshkenbein, A. E. Koshelev, A. I. Larkin, and V. M. Vinokur, Phys. Rev. B **50**, 16770 (1994).

[49] T. Shibauchi, K. Hashimoto, R. Okazaki, and Y. Matsuda, Physica C **469**, 590 (2009); R. Okazaki, M. Konczykowski, C. J. van der Beek, T. Kato, K. Hashimoto, M. Shimozawa, H. Shishido, M. Yamashita, M. Ishikado, H. Kito, A. Iyo, H. Eisaki, S. Shamoto, T. Shibauchi, and Y. Matsuda, Phys. Rev. B **79**, 064520 (2009).

[50] R. Khasanov, D. V. Evtushinsky, A. Amato, H.-H. Klauss, H. Luetkens, Ch. Niedermayer, B. Büchner, G. L. Sun, C. T. Lin, J. T. Park, D. S. Inosov, and V. Hinkov, Phys. Rev. Lett. **102**, 187005 (2009).

[51] R. Prozorov, R. W. Giannetta, A. Carrington, and F. M. Araujo-Moreira, Phys. Rev. B **62**, 115 (2000); R. Prozorov and V. G. Kogan, Rep. Prog. Phys. **74**, 124505 (2011).

[52] P. J. Hirschfeld and N. Goldenfeld, Phys. Rev. B **48**, 4219 (1993).

[53] A. L. Fetter and P. C. Hohenberg, in *Superconductivity*, edited by R. D. Parks (Marcel Dekker, New York, 1967), p. 817.

[54] The geometrical factor G depends on the effective sample size R and on λ_0 as $G \simeq R/\lambda_0$ [51]. The effective size, in turn, is determined by the physical sample size and demagnetization effects. For rectangular samples in the thin-film limit one empirically finds $R \sim w/10$, where w is the width (smaller side) of the rectangle [51]. With an overall sample size of ~ 120 μm this estimate yields a value of G that is about three times larger than found in Fig. 5. We attribute this difference to the fact that our sample has an irregular shape with obtuse and acute corners.

[55] R. Prozorov and R. W. Giannetta, Supercond. Sci. Technol. **19**, R41 (2006).

[56] V. G. Kogan, C. Martin, and R. Prozorov, Phys. Rev. B **80**, 014507 (2009).

[57] D. C. Johnston, Supercond. Sci. Technol. **26**, 115011 (2013).

[58] A. Larkin and A. Varlamov, *Theory of Fluctuations in Superconductors* (Oxford University Press, Oxford, 2005).

[59] C. Chaparro, L. Fang, H. Claus, A. Rydh, G. W. Crabtree, V. Stanev, W. K. Kwok, and U. Welp, Phys. Rev. B **85**, 184525 (2012).

[60] U. Welp, C. Chaparro, A. E. Koshelev, W. K. Kwok, A. Rydh, N. D. Zhigadlo, J. Karpinski, and S. Weyeneth, Phys. Rev. B **83**, 100513 (2011).

[61] Z. Pribulova, T. Klein, J. Kacmarcik, C. Marcenat, M. Konczykowski, S. L. Budko, M. Tillman, and P. C. Canfield, Phys. Rev. B **79**, 020508 (2009); U. Welp, R. Xie, A. E. Koshelev, W. K. Kwok, P. Cheng, L. Fang, and H. H. Wen, *ibid.* **78**, 140510 (2008).

[62] N. Ni, M. E. Tillman, J.-Q. Yan, A. Kracher, S. T. Hannahs, S. L. Bud'ko, and P. C. Canfield, Phys. Rev. B **78**, 214515 (2008); M. Kano, Y. Kohama, D. Graf, F. Balakierev, A. S. Sefat, M. McGuire, B. C. Sales, D. Mandrus, and S. W. Tozer, J. Phys. Soc. Jpn. **78**, 084719 (2009); A. Yamamoto, J. Jaroszynski, C. Tarantini, L. Balicas, J. Jiang, A. Gurevich, D. C. Larbalestier, R. Jin, A. S. Sefat, M. A. McGuire, B. C. Sales, D. K. Christen, and D. Mandrus, Appl. Phys. **94**, 062511 (2009); J. Jaroszynski, F. Hunte, L. Balicas, Youn-jung Jo, I. Raičević, A. Gurevich, D. C. Larbalestier, F. F. Balakirev, L. Fang, P. Cheng, Y. Jia, and H. H. Wen, Phys. Rev. B **78**, 174523 (2008).

[63] A. Gurevich, Phys. Rev. B **67**, 184515 (2003); A. A. Golubov and A. E. Koshelev, *ibid.* **68**, 104503 (2003).